Check for updates

Low-Temperature Sputtered Ultralow-Loss Silicon Nitride for Hybrid Photonic Integration

*Shuangyou Zhang, Toby Bi, Irina Harder, Olga Ohletz, Florentina Gannott, Alexander Gumann, Eduard Butzen, Yaojing Zhang, and Pascal Del'Haye**

Silicon-nitride-on-insulator (Si_3N_4) photonic circuits have seen tremendous advances in many applications, such as on-chip frequency combs, Lidar, telecommunications, and spectroscopy. So far, the best film quality has been achieved with low pressure chemical vapor deposition (LPCVD) and high-temperature annealing (1200°C). However, high processing temperatures pose challenges to the cointegration of Si_3N_4 with pre-processed silicon electronic and photonic devices, lithium niobate on insulator (LNOI), and Ge-on-Si photodiodes. This limits LPCVD as a front-end-of-line process. Here, ultralow-loss Si_3N_4 photonics based on room-temperature reactive sputtering is demonstrated. Propagation losses as low as 5.4 dB m^{-1} after 400°C annealing and 3.5 dB m^{-1} after 800°C annealing are achieved, enabling ring resonators with highest optical quality factors of > 10 million and an average quality factor of 7.5 million. To the best of the knowledge, these are the lowest propagation losses achieved with low temperature Si_3N_4. This ultralow loss enables the generation of microresonator soliton frequency combs with threshold powers of 1.1 mW. The introduced sputtering process offers full complementary metal oxide semiconductor (CMOS) compatibility with front-end silicon electronics and photonics. This could enable hybrid 3D integration of low loss waveguides with integrated lasers and lithium niobate on insulator.

1. Introduction

Benefiting from the maturity, low cost, and scalability of complementary metal-oxide semicondutor (CMOS) manufacturing driven by the microelectronics industry, silicon integrated photonics has enabled significant advances in telecom applications,[1,2] Lidar,[3] integrated photonic sensors,[4] and quantum computing[5,6] over the past decade. Today, silicon photonic integrated circuits have been demonstrated with a wide diversity of optical functions via hybrid integration with different materials, such as III–V-on-Si integrated lasers, Ge-on-Si photodiodes, high-speed modulators, and (de)multiplexers. However, some intrinsic material properties of silicon pose challenges to the performance of silicon optical devices[7] in certain operation regimes. In particular, two-photon absorption of silicon at 1550 nm limits the ability of high-power handling and a high thermo-optic coefficient makes devices sensitive to temperature variations.

Silicon nitride (Si_3N_4) on insulator has attracted intensive interest as a dielectric material platform with ultralow propagation loss for photonic integrated circuits.[8] It has a wide transparency window covering visible to mid-IR, a relatively high nonlinearity (ten times higher than that of silica), and a low thermo-optical coefficient, as well as a CMOS-compatible manufacturing process. With its remarkable progress, it has enabled a wide range of applications in chip-scale frequency combs,[9] Lidar,[10] optical telecommunications,[11] spectroscopy,[12] on-chip delay lines,[13] sensing,[14] just to name a few. Among these applications—in addition to the requirement for low propagation loss—dispersion engineering and high confinement of optical modes is critical, which typically calls for film thicknesses of > 600 nm at telecom wavelengths. High Si_3N_4 thickness results in tight mode confinement in the waveguide core and offers various advantages, including negligible bending losses (small footprint), dispersion engineering capabilities and high effective Kerr nonlinearity. These characteristics are of great importance in nonlinear photonic applications. There are several methods to fabricate thick Si_3N_4 films, such as LPCVD,[15,16] plasma enhanced chemical vapor deposition (PECVD),[17–19] inductively coupled plasma chemical vapor deposition (ICP-CVD),[20] reactive sputtering[21,22] and atomic layer deposition (ALD).[23] So far, the best optical quality of Si_3N_4 films are deposited by high temperature (≈800°C) LPCVD.[8]

S. Zhang, T. Bi, I. Harder, O. Ohletz, F. Gannott, A. Gumann, E. Butzen, Y. Zhang, P. Del'Haye
Max Planck Institute for the Science of Light
91058 Erlangen, Germany
E-mail: pascal.delhaye@mpl.mpg.de

T. Bi, P. Del'Haye
Department of Physics
Friedrich-Alexander-Universität Erlangen-Nürnberg
91058 Erlangen, Germany

The ORCID identification number(s) for the author(s) of this article can be found under https://doi.org/10.1002/lpor.202300642

© 2023 The Authors. Laser & Photonics Reviews published by Wiley-VCH GmbH. This is an open access article under the terms of the Creative Commons Attribution-NonCommercial License, which permits use, distribution and reproduction in any medium, provided the original work is properly cited and is not used for commercial purposes.

DOI: 10.1002/lpor.202300642

However, high film stress resulting from the LPCVD process leads to fatal cracks and prevents thick films (>400 nm) with high optical quality.[15] As a result, several clever and sophisticated processes have been developed, such as patterning crack barriers,[15] multi-step deposition,[15,24,25] and a photonic Damascene process.[26] In particular, prolonged high-temperature annealing (1200°C for >3 h) is indispensable to reduce the material loss and to achieve ultralow propagation loss (≈1 dB m^{-1}). This ultralow loss enables on-chip Si_3N_4 resonators with optical quality factors of >10 million.[24,27,28] However, the high-temperature deposition and annealing processes can cause dopant diffusion and damages prefabricated temperature sensitive devices.[21,29,30] Hence, LPCVD Si_3N_4 is very challenging to use for applications in back-end-of-line (BEOL) fabrication processes, co-integration with front-end-of-the-line (FEOL) silicon optoelectronic circuits, and foundry compatible processes.

In recent years, low-temperature deposited Si_3N_4 films have attracted increasing interest in 3D hybrid integration of Si_3N_4 with other materials.[18,21,29–32] Among different low-temperature deposition methods, PECVD and ICP-CVD are widely used as low-temperature (<400°C), and CMOS compatible processes, providing high-thickness Si_3N_4 films (>1 µm) without cracks. However, the optical loss within the deposited films at telecommunication wavelengths is usually high (typically 200 dB m^{-1}) due to the absorption of Si—H and N—H bonds,[33] which poses a challenge for optical applications. To address this issue, deuterated silane (SiD_4) has been used as the deposition precursor, rather than conventional SiH_4,[29,30,34,35] showing a 10-dB m^{-1} propagation loss. However, SiD_4 precursors are not commonly available in foundries and expensive, which could make this deposition method less attractive for large scale low-loss waveguide fabrication. The state-of-the-art propagation loss with a PECVD process without post thermal annealing is 42 dB m^{-1}, which was achieved recently by including a chemical mechanical planarization step.[36] Another potential BEOL method is low-temperature reactive sputtering of low-loss Si_3N_4 film with low stress.[21,32,37] Waveguide losses of 80 dB m^{-1} at 1550 nm and microring resonators with an intrinsic quality factor of 6×10^5 have been achieved with thermal annealing at 400°C in ambient atmosphere.

Here, we report the realization of ultralow-loss Si_3N_4 photonic devices with high film thickness by reactive sputtering at room temperature. The optical propagation loss of the sputtered Si_3N_4 film is investigated at O-, C-, and L-band wavelength ranges and at different annealing temperatures. After room-temperature sputtering and waveguide fabrication, the Si_3N_4 film loss is 32 dB m^{-1} without thermal annealing and the intrinsic optical quality factor (Q) of the fabricated microresonators is 1.1 million at 1580 nm. After a CMOS-compatible annealing step at a temperature of 400°C, the propagation loss is significantly reduced to 5.4 dB m^{-1} and the resonator Q is improved to 6.2 million at 1580 nm. By additional annealing at 800°C the film quality is further improved, enabling losses of 3.5 dB m^{-1}, with the highest Q-factors beyond 10 million and an average Q-factor of 7.5 million. To demonstrate the viability of the resonators for photonic applications, we show parametric oscillations at threshold powers down to 1.1 mW at 1310 nm. As a further verification of the optical properties of the silicon nitride films, we demonstrate the generation of dissipative Kerr soliton combs centered at both 1.3 µm and 1.5 µm wavelengths. We believe the low-temperature sputtered Si_3N_4 with ultralow optical loss will have a significant impact on scalable foundry photonics and hybrid integration of 3D photonic circuits.

2. Film Deposition and Waveguide Fabrication

Figure 1a shows the fabrication flow starting with a 4-inch silicon wafer with a 3 µm thick thermally oxidized silicon dioxide (SiO_2) layer. The Si_3N_4 film is sputtered at room temperature by a commercial reactive magnetron sputtering system equipped with an asymmetric bipolar pulsed DC source. A P-doped silicon target with a diameter of 2 inch is used as the sputtering source. Pulse power (100-W DC) is used for the Si_3N_4 deposition with a pulse frequency of 50 kHz and a duty cycle of 75%. The sputtering process takes place within a plasma environment containing a mixture of Argon (Ar) and nitrogen (N_2). Argon, with a constant flow rate of 15 sccm serves as the sputtering gas, facilitating the ejection of silicon atoms into the environment through high-energy collisions with the target surface. Throughout the sputtering process, the chamber pressure is controlled at 3 mTorr and the temperature of the sample wafer is not stabilized and remains at ≈ 22°C (see Section S1, Supporting Information, for details). Note that the process is *intrinsically hydrogen free*, which avoids optical losses through N—H or Si—H bonds (see Section S2, Supporting Information, for details). Figure 1b shows the refractive index of the sputtered SiNx film at 636.4 nm as a function of Ar/N_2 ratio, together with a dashed line indicating the refractive index of stoichiometric Si_3N_4.[15] Depending on the targeted refractive index, the Ar/N_2 ratio can be widely tuned, resulting in a variation of the SiNx refractive index from 2.07 (silicon rich) to 2.01 (nitride rich). The refractive index is measured at 636.4 nm with a prism coupler (Metricon 2010 M). For the fabricated samples presented here, the gas ratio is set to ≈ 2.7 for stoichiometric Si_3N_4, and the resulting refractive index is ≈ 2.04 at 636.4 nm with a deposition rate of 130 nm h^{-1}. Figure 1c shows the top surface roughness of the sputtered Si_3N_4 film with a thickness of 750 nm, measured by an atomic-force microscope. The root mean square roughness is 0.26 nm, which is on the same level as that of the substrate. The sputtered Si_3N_4 film is used to fabricate microring resonators to investigate the waveguide propagation loss by measuring the optical quality factor of the resonances and to explore potential applications in nonlinear photonics. A negative-tone photoresist (ma-N 2405) is used to pattern optical waveguides and microrings by electron beam lithography. After developing, the patterned samples are fully etched by inductive coupled plasma reactive ion etching with an etchant mixture of CHF_3 (50 sccm) and O_2 (5 sccm) at a pressure of 15 mTorr and DC bias of 240 V. Figure 1d shows a scanning electron microscope (SEM) image of a 100-µm-radius microring resonator with a waveguide cross-section of 750 nm × 1.8 µm. Figure 1e shows a zoomed-in SEM image of the ring waveguide with no visible sidewall roughness. The gap between the bus waveguide and ring is varied for different coupling conditions at different wavelength ranges. After the Si_3N_4 etching process, piranha solution is used to remove residual photoresist. Following this step, a 3-µm-thickness SiO_2 layer is deposited to encapsulate the samples via two steps. To fill the gap between the bus waveguides and microrings without air voids (see Section S3, Supporting Information, for SEM images of the gap region), a layer of SiO_2 with 400 nm thickness

© 2023 The Authors. Laser & Photonics Reviews published by Wiley-VCH GmbH

18638899, 0, Downloaded from https://onlinelibrary.wiley.com/doi/10.1002/lpor.202300642 by MPI 387 Science of Light, Wiley Online Library on [12/03/2024]. See the Terms and Conditions (https://onlinelibrary.wiley.com/terms-and-conditions) on Wiley Online Library for rules of use; OA articles are governed by the applicable Creative Commons License

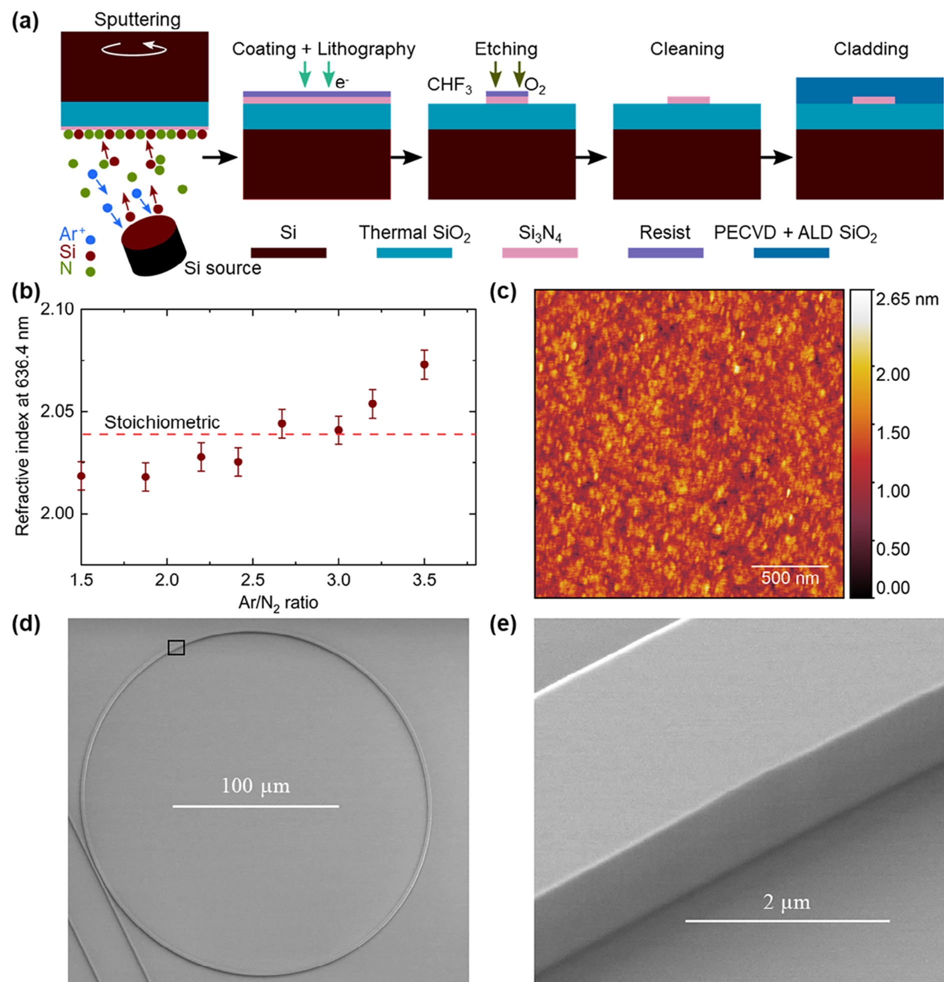

Figure 1. Sputtered Si_3N_4 photonic devices. a) Fabrication flow diagram for sputtered Si_3N_4 photonic devices. b) Refractive index of the sputtered SiNx films as a function of Ar/N_2 ratio measured at 636.4 nm. c) Roughness measurement of the top surface of sputtered Si_3N_4 with 750-nm thickness. d) Scanning electron microscope (SEM) image of a 100-µm-radius microring resonator. e) Zoomed-in (black box in (d)) SEM image of the ring waveguide.

is deposited by ALD at a temperature of 45°C, followed by a 2.5-µm-thickness SiO_2 layer deposited by PECVD at a temperature of 300°C. Due to the tight mode confinement within the Si_3N_4 core, the PECVD SiO_2 layer does not interact significantly with the optical mode, resulting in negligible losses while offering the advantages of cost-effectiveness and a high deposition rate. The samples are diced for end-fire coupling to characterize their optical properties, such as optical Q, propagation loss, and dispersion of microresonators.

3. Characterization of the Sputtered Silicon Nitride Films and Microresonators

As shown in **Figure** 2a, two tunable continuous wave (CW) external cavity diode lasers in the O-band and the C-/L-bands are used to characterize the optical transmission of the sputtered Si_3N_4 microresonators and generate dissipative Kerr soliton microcombs. The polarization of the CW light is aligned by a fiber polarization controller to probe the quasi-transverse electric (TE) or quasi-transverse magnetic (TM) modes of the Si_3N_4 resonators. Light is coupled into and out of the resonators via two lensed fibers. For low coupling loss from fiber to the waveguide, the width of the Si_3N_4 waveguide is tapered down to ≈200 nm (see Section S4, Supporting Information, for details). A coupling loss of < 2 dB per facet is achieved in our experiments. For characterization of the resonators, both CW lasers are set to low optical power to avoid resonance shifts induced by thermal effects and the Kerr effect. The frequency of both CW lasers is widely scanned across a range of 10 THz at a speed of ≈ 1 THz s^{-1}. To determine the laser frequency while scanning, we employ a high-precision calibrated fiber loop cavity for providing frequency markers.[38] The transmission spectra of the Si_3N_4 resonators and reference fiber cavity are simultaneously recorded by an oscilloscope. Further data analysis is used to extract the optical quality factors, propagation loss, and dispersion of the resonators.

3.1. Devices without Thermal Annealing

Figure 2b shows a resonance spectrum of a 200-µm-radius Si_3N_4 resonator at a resonant wavelength of 1318.7 nm, and Figure 2c shows a resonance spectrum of another 200-µm-radius Si_3N_4

© 2023 The Authors. Laser & Photonics Reviews published by Wiley-VCH GmbH

18638899, 0, Downloaded from https://onlinelibrary.wiley.com/doi/10.1002/lpor.202300642 by MPI 387 Science of Light, Wiley Online Library on [12/03/2024]. See the Terms and Conditions (https://onlinelibrary.wiley.com/terms-and-conditions) on Wiley Online Library for rules of use; OA articles are governed by the applicable Creative Commons License

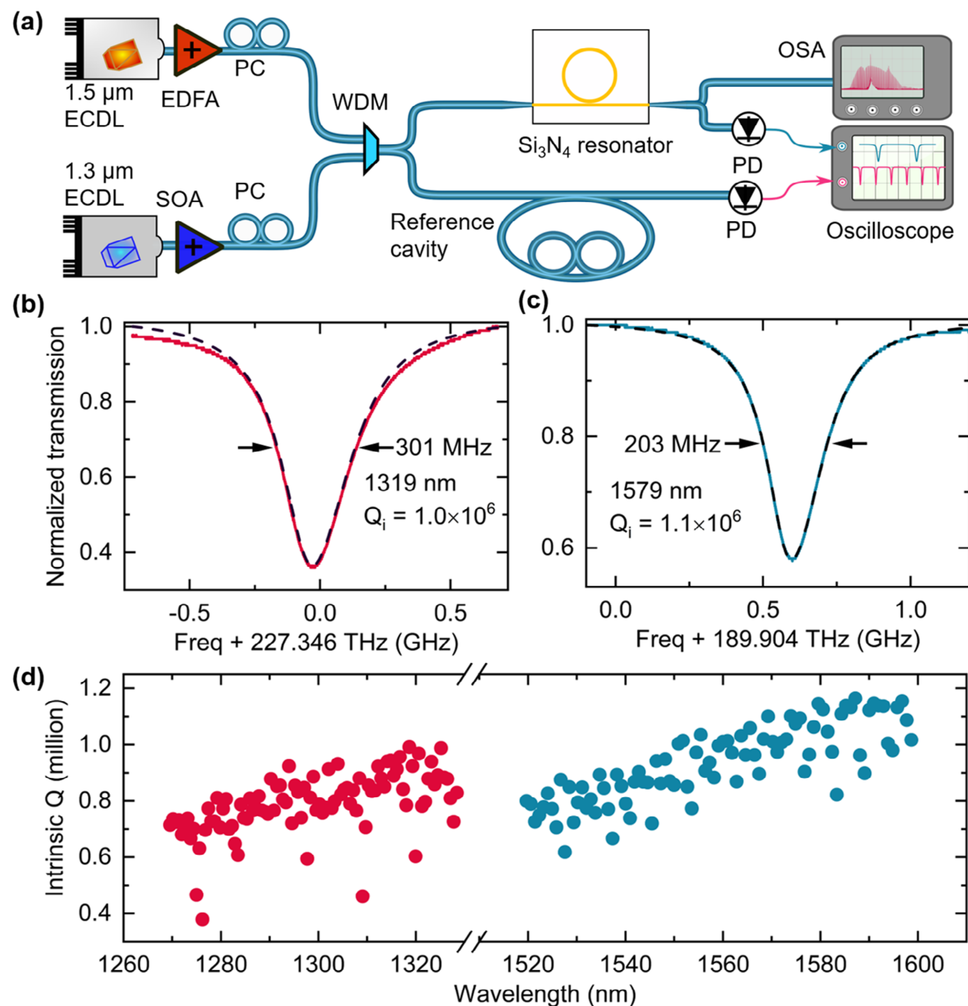

Figure 2. Characterization of sputtered Si_3N_4 resonators without post thermal annealing. a) Experimental setup for characterization of Si_3N_4 resonator transmission spectra, resonator linewidth, optical quality factors, and dispersion. Normalized transmission spectra of Si_3N_4 ring resonators without thermal annealing at 1318 nm b) and 1578 nm c). d) Intrinsic Q measurement of all resonances within the laser wavelength ranges.

resonator at a wavelength of 1578.6 nm. Both resonators are directly fabricated from a room-temperature sputtered film and with silica cladding layers but without post-thermal annealing. The dashed black lines in Figure 2b,c are fitted resonance profiles using extended coupled-mode theory,[39,40] showing that the resonance linewidths at 1319 and 1579 nm are ≈ 300 and 200 MHz, respectively, which correspond to loaded quality factors (Q_l) of 0.75 million at 1319 nm and 0.94 million at 1579 nm. Considering that both resonances are undercoupled, the calculated intrinsic quality factors (Q_i) are 1 million at 1319 nm and 1.1 million at 1579 nm, respectively. The propagation loss α can be estimated from Q_i using $\alpha = f_0/(Q_i \times R \times FSR)$,[41] where f_0 is the resonance frequency, R is the radius of the ring resonator, and FSR is the free spectral range of the microresonator. Without post-thermal annealing, the fabricated sputtered Si_3N_4 can already achieve a propagation loss of 42 dB m^{-1} in the O-band and 32 dB m^{-1} in the L-band. This propagation loss is already lower than that of annealing-free LPCVD Si_3N_4 films deposited at 780°C.[42] Figure 2d shows the distribution of Q_i of the resonances within the measured wavelength range, with an average Q_i of 0.79 ± 0.11 million in the O-band and 0.94 ± 0.13 million across the C- and L-band.

3.2. Devices after 400°C Thermal Annealing

To reduce the material loss, the Si_3N_4 devices after SiO_2 encapsulation are post-processed with thermal annealing. First, we anneal the devices in an ambient atmosphere at 400°C for 8 h. 400°C processing temperature is chosen because it is CMOS compatible and BEOL process compatible, and can be used for the integration of Si_3N_4 with pre-processed CMOS electronics, III–V materials, and prefabricated photonic circuitry, such as lithium niobate on insulator, Ge-on-Si photodiodes, and active silicon modulators. **Figure 3**a,b shows the normalized resonance transmissions of two fundamental TE modes at resonant wavelengths of 1328 and 1610 nm of a 200-μm-radius Si_3N_4 resonator together with fitted line shapes (dashed lines). The loaded resonance linewidth has been dramatically narrowed to ≈ 55 MHz after 400°C annealing, compared to Figure 2b,c. Considering that

© 2023 The Authors. Laser & Photonics Reviews published by Wiley-VCH GmbH

18638899, 0, Downloaded from https://onlinelibrary.wiley.com/doi/10.1002/lpor.202300642 by MPI 387 Science of Light, Wiley Online Library on [12/03/2024]. See the Terms and Conditions (https://onlinelibrary.wiley.com/terms-and-conditions) on Wiley Online Library for rules of use; OA articles are governed by the applicable Creative Commons License

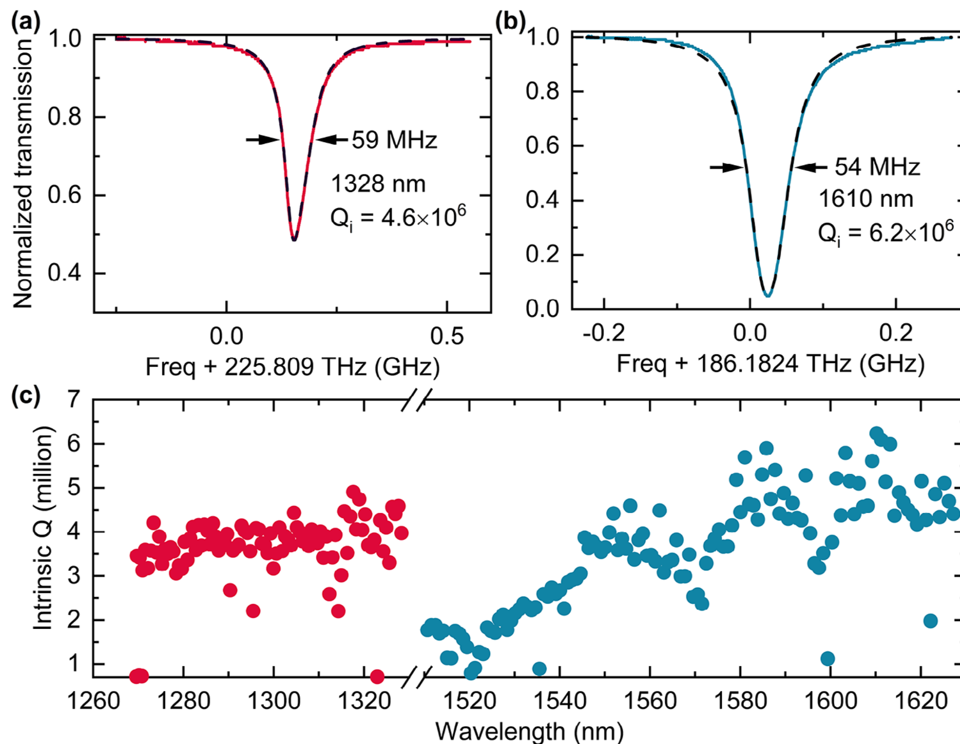

Figure 3. Q measurement of a 200-µm-radius Si_3N_4 ring resonator after 400°C thermal annealing. Normalized transmission spectra of a fundamental TE mode at 1328 nm a) and a fundamental TE mode at 1610 nm b) in a 200-µm-radius ring resonator. c) Intrinsic Q measurement of fundamental TE modes within the laser wavelength ranges in the O- and C/L-band.

the device is designed for undercoupling across the measurement range, the calculated intrinsic Qs at 1328 and 1610 nm are 4.6 and 6.2 million, respectively, corresponding to a propagation loss of 9.0 dB m^{-1} at 1328 nm and 5.4 dB m^{-1} at 1610 nm. This is approximately a fivefold improvement compared to the propagation loss without thermal annealing. Figure 3c shows the distribution of the intrinsic Qs of the fundamental TE mode of the resonator under test covering the O- and C+L-band wavelength ranges. The intrinsic propagation loss in the O-band stays roughly constant with an average Q_i of 3.8 ± 0.7 million. We observe some low Q modes, which are a result of mode crossings (see Section S5, Supporting Information, for details). In comparison, the intrinsic loss in the C-band is slightly higher than in the L-band, which we speculate is due to residual losses in the material (see Section S2, Supporting Information, for details). An average Q_i of 3.6 ± 1.3 million is measured across the C- and L-band. To the best of our knowledge, this is the lowest Si_3N_4 propagation loss reported with a peak processing temperature of 400°C.

3.3. Devices after 800°C Thermal Annealing

To further reduce the material loss of the sputtered Si_3N_4 film, we anneal the devices at a higher temperature of 800°C. This processing temperature can enable future integration of sputtered Si_3N_4 with silicon integrated photonics, such as Si modulators[43] and Ge-on-Si photodiodes.[44] After encapsulation, the devices are post-annealed at 800°C for 8 h. **Figure 4a** shows a normalized resonance transmission of a 200-µm-radius Si_3N_4 resonator at a resonance wavelength of 1319 nm where the resonance is close to critically coupled but still undercoupled, together with a fitted line shape (dashed line). The loaded resonance linewidth is ≈ 37.5 MHz. The calculated loaded and intrinsic Qs are 6.1 million and 9.2 million, respectively, corresponding to a propagation loss of 4.5 dB m^{-1}. The losses at 1319 nm are approximately halved compared with the losses after 400°C thermal annealing. Figure 4b shows the distribution of the intrinsic Qs of the fundamental TE mode of the resonator in different wavelength ranges. From Figure 4b, we note that the intrinsic Q of some modes in the L-band is beyond 10 million, and the corresponding propagation loss is < 3.5 dB m^{-1}. See Section S6 (Supporting Information) for the normalized resonance transmission in L-band. Similar to Figure 2c, the intrinsic propagation loss in the O-band stays nearly constant with an average intrinsic Q of 7.0 ± 1.8 million, except for a few low-Q modes resulting from mode crossings. The intrinsic Q distribution in the C- and L-bands is significantly different from the Q distribution in Figure 3c. After 800°C thermal annealing, the intrinsic losses in the C- and L-bands are roughly constant as shown in Figure 4b. This shows that the material loss in the C-band has been effectively reduced by 800°C annealing. The average intrinsic Q crossing the C- and L-bands is 7.5 ± 2.2 million. In **Figure 5**, we compare our results with other state-of-the-art low-temperature Si_3N_4 deposition methods with high film thickness (> 600 nm). To the best of our knowledge, this is the lowest Si_3N_4 propagation loss reported at a peak processing temperature of 800°C. To further verify the ultrahigh optical Q of our Si_3N_4 ring resonators, we test the threshold optical power for

© 2023 The Authors. Laser & Photonics Reviews published by Wiley-VCH GmbH
18638899, 0, Downloaded from https://onlinelibrary.wiley.com/doi/10.1002/lpor.202300642 by MPI 387 Science of Light, Wiley Online Library on [12/03/2024]. See the Terms and Conditions (https://onlinelibrary.wiley.com/terms-and-conditions) on Wiley Online Library for rules of use; OA articles are governed by the applicable Creative Commons License

18638899, 0, Downloaded from https://onlinelibrary.wiley.com/doi/10.1002/lpor.202300642 by MPI 387 Science of Light, Wiley Online Library on [12/03/2024]. See the Terms and Conditions (https://onlinelibrary.wiley.com/terms-and-conditions) on Wiley Online Library for rules of use; OA articles are governed by the applicable Creative Commons License

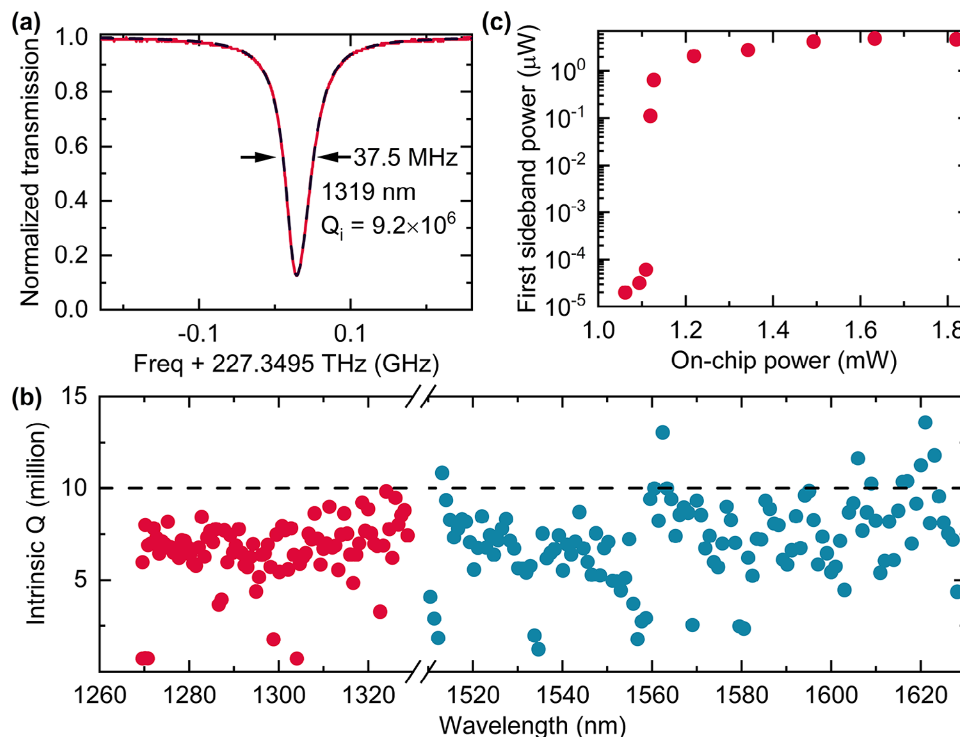

Figure 4. Q measurement of devices after 800°C thermal annealing. a) Normalized transmission spectrum of a fundamental TE mode at 1319 nm in a 200-μm-radius ring resonator. b) Intrinsic Q measurement of the fundamental TE modes in the O-, C-, and L-bands. c) Optical parametric oscillation threshold power measurement for a 130-μm-radius ring resonator.

Kerr-nonlinear optical parametric oscillations (OPO). The threshold power is determined by measuring the optical power in one of the two generated optical sidebands when varying the on-chip optical power. Figure 4c shows experimental results when pumping an optical mode at 1312 nm in a 130-μm-radius ring resonator with a loaded Q of 5.5 million and an intrinsic Q of 9 million, showing a threshold power of ≈1.1 mW. With an effective area of the pump mode $A_{eff} = 0.99$ μm^2 (obtained from a COMSOL Multiphysics simulation) and the Kerr nonlinear coefficient $n_2 = 2.4\times10^{-19}$ m^2 W^{-1},[27] the calculated threshold power is 1.06 mW, agreeing well with the observed threshold power of 1.1 mW.

In addition to the OPO threshold power measurement, we employ a recently developed method[45] to explore the material-loss-limited Q factors in the sputtered microresonators after 800°C annealing. We conduct measurements to investigate the resonance shift in response to changes in the intracavity circulating optical power and microresonator temperature change. Moreover, we measure the resonance shift ratio between Kerr effect and photothermal effects. Based on results using finite-element method simulations (COMSOL Multiphysics), we have determined the material-loss-limited Q factors of our resonators to be ≈ 20.5 ± 1.9 million after 800°C annealing at a wavelength of 1550 nm. See Section S7, Supporting Information, for detailed experiments and simulations. This value exceeds the presented intrinsic optical quality factor. Thus, we expect that a reduction of surface roughness can further reduce optical losses in our Si_3N_4 structures. This aligns with findings from existing literature.[27,45] Our measurements reveal that scattering losses impose a limitation of ≈10 million on the optical quality factor. Given that the annealing process at lower temperatures does not effectively mitigate scattering losses, especially considering the relatively mild thermal treatment (<400°C) employed in our study, which is significantly lower than the Si_3N_4 softening temperature (1900°C), we assume that the quality factors at temperatures < 400°C are primarily limited by material loss.

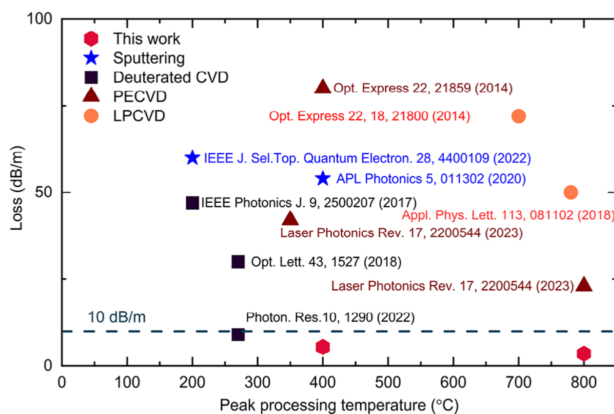

Figure 5. Propagation loss comparison with other state-of-the-art research based on low-temperature silicon nitride deposition techniques with high film thickness (>600 nm), including annealing-free LPCVD, PECVD, sputtering, and deuterated silicon nitride based on ICP-CVD. Our structures have been annealed in ambient atmosphere for 8 h.

 © 2023 The Authors. Laser & Photonics Reviews published by Wiley-VCH GmbH

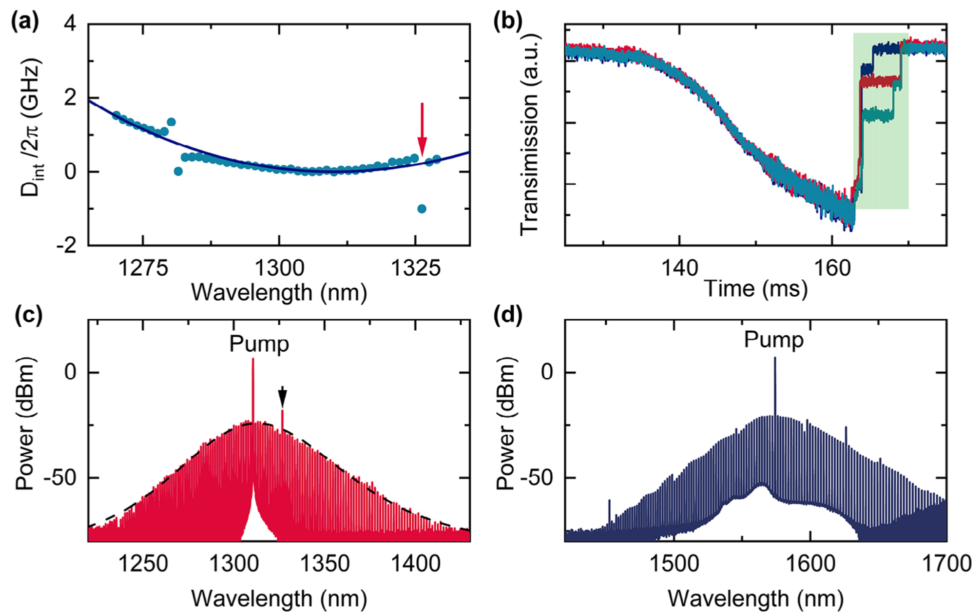

Figure 6. Soliton frequency comb generation in sputtered Si_3N_4 resonators. a) Measured integrated dispersion profile (blue circles) at a pump wavelength of 1310 nm together with a second-order polynomial fit (blue trace). b) Measured transmission traces when scanning the 1.3-µm pump laser frequency from the blue-detuned to the red-detuned side of the resonance. c) Optical spectrum of a soliton frequency comb generated in the sputtered Si_3N_4 resonator pumped at 1310 nm and a $sech^2$ envelope fit (black dashed trace). d) Optical spectrum of a soliton frequency comb pumped at 1574 nm.

4. Soliton Frequency Comb Generation in Sputtered Si_3N_4

In this section, we use the fabricated Si_3N_4 microresonators for soliton frequency comb generation. We first measure the dispersion of a 100-µm-radius resonator with a cross-section of 750 nm × 1.8 µm. The resonance frequencies of a mode family in a resonator can be described with a Taylor series as[26,46]

$$\omega_\mu = \omega_0 + D_1\mu + \frac{D_2}{2!}\mu^2 + \cdots = \omega_0 + D_1\mu + D_{int}(\mu) \quad (1)$$

where μ is the mode number offset from the center mode at $\mu = 0$ and ω_μ are the resonance frequencies. $D_1/2\pi$ is the FSR of the resonator at the center mode ($\mu = 0$), and D_2 is the coefficient of second-order dispersion. D_{int} is the integrated dispersion, depicting the deviation of resonance frequencies from the equidistant grid spaced by D_1. **Figure 6a** shows the measured integrated dispersion profile (blue circles) at a center mode of 1310 nm together with a second-order polynomial fitted curve (blue curve). The dispersion profile shows anomalous dispersion with mode crossings at 1280 and 1326 nm and is suitable for bright soliton generation. We test this Si_3N_4 resonator for the generation of a bright soliton frequency comb by pumping a mode at 1310 nm. The experimental setup is shown in Figure 2a. Previously, for characterizing the resonators, both lasers were operated at very low optical power. During soliton generation, we increase the power of both lasers to ≈100 mW. To overcome the thermal effect of the microresonator, the 1.55-µm laser is simultaneously coupled into a resonance to thermally stabilize the intracavity power.[47] Figure 6b shows the transmission traces when scanning the 1.3-µm pump laser across the resonance from the blue- to the red-detuned side. Different soliton steps, corresponding to different soliton numbers, are observed in the red-detuned regime (green shaded area).[47,48] Using the passive temperature stabilization with the auxiliary laser at 1.55 µm, bright solitons at 1.31 µm can be accessed by manually tuning the laser frequency into the red-detuned soliton regime. Pumping with 80 mW on-chip power at 1.3 µm wavelength leads to the generation of a bright soliton, shown in Figure 6c together with a fitted $sech^2$ envelope (black dashed). Note that the mode crossing at 1326 nm (c.f. dispersion profile in Figure 6a) induces a dispersive wave (marked with an arrow) at 1326 nm in Figure 6c. In addition, we also demonstrate a bright soliton frequency comb at 1.55 µm. Figure 6d shows an optical spectrum of a bright single soliton when pumping a mode at 1574 nm. See Section S8 (Supporting Information) for the measured integrated dispersion profile at 1574 nm. In this case, the 1.3-µm laser is used as the auxiliary laser to thermally stabilize the resonator.

5. Conclusion

In summary, we report the fabrication of ultralow-loss Si_3N_4 photonics with high film thickness using room-temperature reactive sputtering. The measured propagation loss is 32 dB m^{-1} without post-thermal annealing. After thermal annealing at a CMOS-compatible processing temperature (400°C), the film loss is dramatically reduced to 5.4 dB m^{-1}, enabling the fabrication of Si_3N_4 ring resonators with an intrinsic Q of 6.2 million in the L-band. The deposition process is intrinsically hydrogen free, which prevents the formation of optically lossy hydrogen bonds. Ultralow loss integrated Si_3N_4 devices with low temperature

© 2023 The Authors. Laser & Photonics Reviews published by Wiley-VCH GmbH

18638899, 0, Downloaded from https://onlinelibrary.wiley.com/doi/10.1002/lpor.202300642 by MPI 387 Science of Light, Wiley Online Library on [12/03/2024]. See the Terms and Conditions (https://onlinelibrary.wiley.com/terms-and-conditions) on Wiley Online Library for rules of use; OA articles are governed by the applicable Creative Commons License

annealing enable fully monolithic back end of line integration with pre-processed CMOS electronics, silicon integrated photonics,[7] and LNOI.[49] After further thermal annealing at 800°C, the film losses are further reduced to 3.5 dB m^{-1} corresponding to attainable optical quality factors of microresonators beyond 10 million. This performance is also the lowest Si_3N_4 propagation loss reported at a peak processing temperature of 800°C. We believe that our low-temperature sputtered Si_3N_4 is a significant step toward the hybrid monolithic integration of silicon nitride with silicon photonics for applications in telecom systems, nonlinear optics, frequency comb generation and scaling of quantum computing systems.[50]

Supporting Information

Supporting Information is available from the Wiley Online Library or from the author.

Acknowledgements

This work was supported by the European Union's H2020 ERC Starting Grant "CounterLight" 756966; H2020 Marie Sklodowska-Curie COFUND "Multiply" 713694; Marie Curie Innovative Training Network "Microcombs" 812818; and the Max Planck Society. The authors would like to thank Prof. Victor Torres-Company and Krishna Twayana for helpful discussions.

Open access funding enabled and organized by Projekt DEAL.

Conflict of Interest

The authors declare no conflict of interest.

Data Availability Statement

The data that support the findings of this study are available from the corresponding author upon reasonable request.

Keywords

hybrid photonic integration, low-temperature sputtering, silicon nitride, soliton frequency comb

Received: July 14, 2023
Revised: December 19, 2023
Published online:

[1] A. H. Atabaki, S. Moazeni, F. Pavanello, H. Gevorgyan, J. Notaros, L. Alloatti, M. T. Wade, C. Sun, S. A. Kruger, H. Meng, K. Al Qubaisi, I. Wang, B. Zhang, A. Khilo, C. V. Baiocco, M. A. Popovic, V. M. Stojanovic, R. J. Ram, *Nature* **2018**, *556*, 349.
[2] W. Bogaerts, L. Chrostowski, *Laser Photonics Rev.* **2018**, *12*, 1700237.
[3] F. Falconi, S. Melo, F. Scotti, M. N. Malik, M. Scaffardi, C. Porzi, L. Ansalone, P. Ghelfi, A. Bogoni, *J. Lightwave Technol.* **2021**, *39*, 17.
[4] J. Milvich, D. Kohler, W. Freude, C. Koos, *Adv. Opt. Photon.* **2021**, *13*, 584.
[5] X. Qiang, Y. Wang, S. Xue, R. Ge, L. Chen, Y. Liu, A. Huang, X. Fu, P. Xu, T. Yi, F. Xu, M. Deng, J. B. Wang, J. D. A. Meinecke, J. C. F. Matthews, X. Cai, X. Yang, J. Wu, *Sci. Adv.* **2021**, *7*, eabb8375.
[6] X. Li, N. Youngblood, Z. Cheng, S. G.-C. Carrillo, E. Gemo, W. H. P. Pernice, C. D. Wright, H. Bhaskaran, *Optica* **2020**, *7*, 218.
[7] W. D. Sacher, J. C. Mikkelsen, Y. Huang, J. C. C. Mak, Z. Yong, X. Luo, Y. Li, P. Dumais, J. Jiang, D. Goodwill, E. Bernier, P. G. Lo, J. K. S. Poon, *Proc. IEEE* **2018**, *106*, 2232.
[8] X. Ji, S. Roberts, M. Corato-Zanarella, M. Lipson, *APL Photonics* **2021**, *6*, 071101.
[9] B. Stern, X. Ji, Y. Okawachi, A. L. Gaeta, M. Lipson, *Nature* **2018**, *562*, 401.
[10] P. Trocha, M. Karpov, D. Ganin, M. H. P. Pfeiffer, A. Kordts, S. Wolf, J. Krockenberger, P. Marin-Palomo, C. Weimann, S. Randel, W. Freude, T. J. Kippenberg, C. Koos, *Science* **2018**, *359*, 887.
[11] J. Pfeifle, V. Brasch, M. Lauermann, Y. Yu, D. Wegner, T. Herr, K. Hartinger, P. Schindler, J. Li, D. Hillerkuss, R. Schmogrow, C. Weimann, R. Holzwarth, W. Freude, J. Leuthold, T. J. Kippenberg, C. Koos, *Nat. Photonics* **2014**, *8*, 375.
[12] A. Dutt, C. Joshi, X. Ji, J. Cardenas, Y. Okawachi, K. Luke, A. L. Gaeta, M. Lipson, *Sci. Adv.* **2018**, *4*, e1701858.
[13] C. Xiang, M. L. Davenport, J. B. Khurgin, P. A. Morton, J. E. Bowers, *IEEE J. Sel. Top. Quantum Electron.* **2018**, *24*, 1.
[14] P. Muellner, E. Melnik, G. Koppitsch, J. Kraft, F. Schrank, R. Hainberger, *Procedia Eng* **2015**, *120*, 578.
[15] K. Luke, A. Dutt, C. B. Poitras, M. Lipson, *Opt. Express* **2013**, *21*, 22829.
[16] H. Zhang, C. Li, X. Tu, J. Song, H. Zhou, X. Luo, Y. Huang, M. Yu, G. Q. Lo, *Opt. Express* **2014**, *22*, 21800.
[17] I. Kobayashi, T. O. Tetsu Ogawa, S. H. Sadayoshi Hotta, *Jpn. J. Appl. Phys.* **1992**, *31*, 336.
[18] W. D. Sacher, Y. Huang, G.-Q. Lo, J. K. S. Poon, *J. Lightwave Technol.* **2015**, *33*, 901.
[19] Y. Huang, J. Song, X. Luo, T.-Y. Liow, G.-Q. Lo, *Opt. Express* **2014**, *22*, 21859.
[20] J. Yota, J. Hander, A. A. Saleh, *J. Vac. Sci. Technol. A* **2000**, *18*, 372.
[21] A. Frigg, A. Boes, G. Ren, I. Abdo, D.-Y. Choi, S. Gees, A. Mitchell, *Opt. Express* **2019**, *27*, 37795.
[22] S. Schmidt, T. Hänninen, J. Wissting, L. Hultman, N. Goebbels, A. Santana, M. Tobler, H. Högberg, *J. Appl. Phys.* **2017**, *121*, 171904.
[23] X. Meng, Y.-C. Byun, H. Kim, J. Lee, A. Lucero, L. Cheng, J. Kim, *Materials* **2016**, *9*, 1007.
[24] Z. Ye, K. Twayana, P. A. Andrekson, V. Torres-Company, *Opt. Express* **2019**, *27*, 35719.
[25] H. El Dirani, L. Youssef, C. Petit-Etienne, S. Kerdiles, P. Grosse, C. Monat, E. Pargon, C. Sciancalepore, *Opt. Express* **2019**, *27*, 30726.
[26] M. H. P. Pfeiffer, A. Kordts, V. Brasch, M. Zervas, M. Geiselmann, J. D. Jost, T. J. Kippenberg, *Optica* **2016**, *3*, 20.
[27] X. Ji, F. A. S. Barbosa, S. P. Roberts, A. Dutt, J. Cardenas, Y. Okawachi, A. Bryant, A. L. Gaeta, M. Lipson, *Optica* **2017**, *4*, 619.
[28] J. Liu, A. S. Raja, M. Karpov, B. Ghadiani, M. H. P. Pfeiffer, B. Du, N. J. Engelsen, H. Guo, M. Zervas, T. J. Kippenberg, *Optica* **2018**, *5*, 1347.
[29] T. Hiraki, T. Aihara, H. Nishi, T. Tsuchizawa, *IEEE Photonics J* **2017**, *9*, 1.
[30] J. Chiles, N. Nader, D. D. Hickstein, S. P. Yu, T. C. Briles, D. Carlson, H. Jung, J. M. Shainline, S. Diddams, S. B. Papp, S. W. Nam, R. P. Mirin, *Opt. Lett.* **2018**, *43*, 1527.
[31] Z. Wu, Y. Zhang, S. Zeng, J. Li, Y. Xie, Y. Chen, S. Yu, *Opt. Express* **2021**, *29*, 29557.
[32] A. Frigg, A. Boes, G. Ren, T. G. Nguyen, D.-Y. Choi, S. Gees, D. Moss, A. Mitchell, *APL Photonics* **2020**, *5*, 011302.
[33] S. C. Mao, S. H. Tao, Y. L. Xu, X. W. Sun, M. B. Yu, G. Q. Lo, D. L. Kwong, *Opt. Express* **2008**, *16*, 20809.

© 2023 The Authors. Laser & Photonics Reviews published by Wiley-VCH GmbH

18638899, 0, Downloaded from https://onlinelibrary.wiley.com/doi/10.1002/lpor.202300642 by MPI 387 Science of Light, Wiley Online Library on [12/03/2024]. See the Terms and Conditions (https://onlinelibrary.wiley.com/terms-and-conditions) on Wiley Online Library for rules of use; OA articles are governed by the applicable Creative Commons License

[34] Y. Xie, J. Li, Y. Zhang, Z. Wu, S. Zeng, S. Lin, Z. Wu, W. Zhou, Y. Chen, S. Yu, *Photon. Res.* **2022**, *10*, 1290.
[35] D. Bose, J. Wang, D. J. Blumenthal, in *Conf. on Lasers and Electro-Optics* **2022**, *Paper SF3O.1*, Optica Publishing Group, NW Washington, DC **2022**.
[36] X. Ji, Y. Okawachi, A. Gil-Molina, M. Corato-Zanarella, S. Roberts, A. L. Gaeta, M. Lipson, *Laser Photonics Rev.* **2023**, *17*, 2200544.
[37] R. Tsuchiya, R. Oyamada, T. Fukushima, J. A. Piedra-Lorenzana, T. Hizawa, T. Nakai, Y. Ishikawa, *IEEE J. Sel. Top. Quantum Electron.* **2022**, *28*, 1.
[38] S. Zhang, T. Bi, P. Del'Haye, **2023**, arXiv:2303.14180.
[39] Q. Li, A. A. Eftekhar, Z. Xia, A. Adibi, *Phys. Rev. A* **2013**, *88*, 033816.
[40] M. H. P. Pfeiffer, J. Liu, A. S. Raja, T. Morais, B. Ghadiani, T. J. Kippenberg, *Optica* **2018**, *5*, 884.
[41] P. Rabiei, W. H. Steier, C. Zhang, L. R. Dalton, *J. Lightwave Technol.* **2002**, *20*, 1968.
[42] H. El Dirani, A. Kamel, M. Casale, S. Kerdiles, C. Monat, X. Letartre, M. Pu, L. K. Oxenløwe, K. Yvind, C. Sciancalepore, *Appl. Phys. Lett.* **2018**, *113*, 081102.
[43] M. Streshinsky, R. Ding, Y. Liu, A. Novack, Y. Yang, Y. Ma, X. Tu, E. K. S. Chee, A. E.-J. Lim, P. G. Lo, T. Baehr-Jones, M. Hochberg, *Opt. Express* **2013**, *21*, 30350.
[44] J. Michel, J. Liu, L. C. Kimerling, *Nat. Photonics* **2010**, *4*, 527.
[45] M. Gao, Q.-F. Yang, Q.-X. Ji, H. Wang, L. Wu, B. Shen, J. Liu, G. Huang, L. Chang, W. Xie, S.-P. Yu, S. B. Papp, J. E. Bowers, T. J. Kippenberg, K. J. Vahala, *Nat. Commun.* **2022**, *13*, 3323.
[46] S. Zhang, J. M. Silver, T. Bi, P. Del'haye, *Nat. Commun.* **2020**, *11*, 6384.
[47] S. Zhang, J. M. Silver, L. Del Bino, F. Copie, M. T. M. Woodley, G. N. Ghalanos, A. Ø. Svela, N. Moroney, P. Del'haye, *Optica* **2019**, *6*, 206.
[48] T. Herr, V. Brasch, J. D. Jost, C. Y. Wang, N. M. Kondratiev, M. L. Gorodetsky, T. J. Kippenberg, *Nat. Photonics* **2014**, *8*, 145.
[49] X. Han, Y. Jiang, A. Frigg, H. Xiao, P. Zhang, T. G. Nguyen, A. Boes, J. Yang, G. Ren, Y. Su, A. Mitchell, Y. Tian, *Laser Photonics Rev.* **2022**, *16*, 2100529.
[50] K. K. Mehta, C. Zhang, M. Malinowski, T.-L. Nguyen, M. Stadler, J. P. Home, *Nature* **2020**, *586*, 533.

© 2023 The Authors. Laser & Photonics Reviews published by Wiley-VCH GmbH

18638899, 0, Downloaded from https://onlinelibrary.wiley.com/doi/10.1002/lpor.202300642 by MPI 387 Science of Light, Wiley Online Library on [12/03/2024]. See the Terms and Conditions (https://onlinelibrary.wiley.com/terms-and-conditions) on Wiley Online Library for rules of use; OA articles are governed by the applicable Creative Commons License